Materials Today Bio 32 (2025) 101757

Contents lists available at ScienceDirect

Materials Today Bio

journal homepage: www.journals.elsevier.com/materials-today-bio

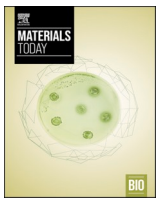

ROS-responsive drug delivery system with enhanced anti-angiogenic and anti-inflammatory properties for neovascular age-related macular degeneration therapy

Jiayi Zuo [a,b,1], Yining Pan [a,b,1], Yuanli Wang [a,b,1], Wei Wang [a,b], Haojie Zhang [a,b], Si Zhang [c], Youru Wu [a,b], Jiangfan Chen [a,b,**], Qingqing Yao [a,b,*]

[a] State Key Laboratory of Eye Health, Optometry and Vision Science, Eye Hospital, Wenzhou Medical University, Wenzhou, 325027, China
[b] Zhejiang Key Laboratory of Key Technologies for Visual Pathway Reconstruction, Eye Hospital, Wenzhou Medical University, Wenzhou, 325027, China
[c] Department of Ophthalmology, The First People's Hospital of Foshan, Foshan, Guangdong 528000, China

ARTICLE INFO

Keywords:
Age-related macular degeneration
Integrated nano-drug delivery system
Yes-associated protein-1
Anti-angiogenic
ROS-Scavenging

ABSTRACT

Neovascular age-related macular degeneration (nAMD) has become the leading cause of vision loss in people over 60 years old. Anti–vascular endothelial growth factor (anti-VEGF), the current first-line drug for the treatment of nAMD, suffers from poor patient compliance and fundus fibrosis scar formation. In addition to VEGF, oxidative stress and inflammation also play key roles in the pathological process of choroidal neovascularization (CNV). Therefore, combinational therapeutics with anti-angiogenic, reactive oxygen species (ROS)-scavenging and anti-inflammatory functions will broaden therapeutic effects and reduce side effects. The Yes-associated protein-1 (YAP) has proven to inhibit angiogenesis, inflammation, and subretinal fibrosis in CNV. Herein, verteporfin (VP), the inhibitor of YAP, was encapsulated into a polydopamine modified mesoporous silica nanoparticle (PMSN-VP NPs) and then conjugated with PLGA-PEG-PBA decorated cerium oxide nanoparticles ($PPCeO_2$ NPs) to develop an integrated nano-drug delivery system. The PMSN-VP@$PPCeO_2$ NPs exhibited ROS-responsive degradation and VP release behaviors, and our *in vitro* data revealed that the PMSN-VP@$PPCeO_2$ NPs downregulated angiogenic-related and fibrosis-related gene expressions in human umbilical vein endothelial cells (HUVECs) and further showed excellent anti-oxidative and anti-inflammatory capacities in BV2 cells. More importantly, the PMSN-VP@$PPCeO_2$ NPs significantly suppressed vascular leakage and macrophage infiltration in the laser-induced CNV lesions of mice. Overall, our findings demonstrated that the PMSN-VP@$PPCeO_2$ NPs provided an effective therapeutic strategy for nAMD.

1. Introduction

Age-related macular degeneration (AMD), characterized by the progressive degenerative disease of the macula, is the leading cause of vision loss in people older than 60 years, accounting for 8.7 % of all blindness worldwide [1,2]. By 2040, ~288 million people will suffer from AMD globally [1]. The late stage of AMD is classified into two subtypes: geographic atrophy (GA) and neovascular AMD (nAMD, also known as wet AMD). In nAMD, abnormal choroidal neovascular growth into the sub-retinal space disrupts Bruch's membrane and the RPE layer, eventually resulting in detachment of the retina and vision loss [3]. Though nAMD accounts for approximately 10–15 % of patients diagnosed with AMD, nearly 90 % of severe vision loss is caused by nAMD.

Choroidal neovascularization (CNV) is the key pathological feature of nAMD, and intravitreal anti-vascular endothelial growth factor (VEGF) agents are currently the first-line therapy for nAMD, but they suffer from issues related to patient compliance and fundus fibrosis scar formation [4]. Recently, a series of studies have reported that oxidative

* Corresponding author. School of Ophthalmology & Optometry, Eye Hospital, Wenzhou Medical University, 270 Xueyuan Xi Road, Wenzhou, Zhejiang, 325027, , China.
** Corresponding author. School of Ophthalmology & Optometry, Eye Hospital, Wenzhou Medical University, 270 Xueyuan Xi Road, Wenzhou, Zhejiang, 325027, , China.
E-mail addresses: chenjf555@gmail.com (J. Chen), qingqingyao@wmu.edu.cn (Q. Yao).
[1] These authors contributed equally to this manuscript.

https://doi.org/10.1016/j.mtbio.2025.101757
Received 29 September 2024; Received in revised form 5 April 2025; Accepted 9 April 2025
Available online 10 April 2025

stress and inflammation also play crucial roles in the pathogenesis of AMD [5–7]. For instance, Farrokhran et al. reported that oxidative stress and hypoxia synergistically stimulated HIF-1α accumulation in the RPE, leading to increased expression of HIF-1α-dependent angiogenic factors and promoting the development of CNV [8]. Terao et al. found that oxidative stress can promote inflammatory response by activating the nuclear factor-κB (NF-κB) signaling pathway [9]. Moreover, macrophages/microglia and lymphocytes were observed in the activated CNV lesions, pro-inflammatory cytokine levels were elevated, and the complement system was activated [10]. Additionally, the inflammatory factors further promoted VEGF secretion, leading to the formation of pathological CNV [11]. Overall, VEGF, ROS, and inflammation together contribute to the pathological CNV formation, and the development of alternative therapeutic strategies that combine anti-VEGF, ROS-scavenging, and anti-inflammatory functions is highly desired for clinical CNV treatment.

The Yes-associated protein (YAP) *and transcriptional co-activator PDZ binding motif (TAZ)* **are the most important downstream effectors** in the Hippo pathway cascade, which have been demonstrated to regulate endothelial cell proliferation, migration, and survival, subsequently regulating vascular formation and remodeling [12–14]. Since the inhibition of the Hippo pathway can activate YAP and TAZ, the active YAP/TAZ then translocates to the nucleus and binds to TEA domain family member (TEAD) transcription factors and mediates pro-angiogenic gene expression, such as cysteine-rich angiogenic inducer 61 (CYR61), connective tissue growth factor (CTGF), VEGF, angiopoietin-2 (Ang-2), and so on [15–17]. Ang-2 binds with the receptor tyrosine kinase Tie2 in endothelial cells and is a key regulator in *vascular* maturation and homeostasis [18]. Kim et al. reported that Ang-2 participates in vascular leakage and abnormal changes in vascular structure in CNV, and also increases pro-inflammatory factor expression [19]. In addition, Wang et al. found that VEGF-VEGFR2 signaling regulates YAP/TAZ activity during angiogenesis via remodeling of the actin cytoskeleton [20]. More importantly, the accumulation of reactive oxygen species (ROS) elevates TGF-β2-induced YAP dephosphorylation in endothelial cells, which in turn promotes endothelial-to-mesenchymal transition (EndoMT), subretinal fibrosis, and inflammation in CNV [21]. Overall, the Hippo-YAP signaling pathway is involved in the formation of choroidal neovascularization (CNV), and subretinal fibrosis that is caused by various pathological factors such as VEGF, Ang-2, reactive oxygen species (ROS), and inflammation. We propose that targeted regulation of the Hippo-YAP signaling is the key to the treatment of nAMD.

Verteporfin (VP), the second-generation porphyrin photosensitizer, is clinically used for photodynamic therapy to treat AMD [22]. However, its application in clinics has been limited by super-physiologic dose requirements, injection site reactions and visual disturbances [23]. Additionally, VP is also an inhibitor of YAP and could inhibit YAP nuclear translocation, thereby downregulating angiogenic-related factor expressions [24,25]. Cerium oxide nanoparticles (CeO_2 NPs) are emerging nanoenzymes owing to the co-existence of Ce^{3+} and Ce^{4+} atoms and large numbers of oxygen vacancies on their surfaces [26,27]. The superoxide dismutase (SOD) and catalase (CAT) activities of CeO_2 NPs endow the ROS-scavenging and anti-inflammatory capabilities [28,29]. Moreover, studies report that the catalytic activity of CeO_2 NPs can be enhanced by enlarging their surface area and increasing the ratio of Ce^{3+} [30,31].

Therefore, in this work, VP was encapsulated into a polydopamine modified mesoporous silica nanoparticle (PMSN-VP) and grafted with PLGA-PEG-PBA wrapped CeO_2 ($PPCeO_2$) through the boric acid ester bond. Under the high ROS levels pathological microenvironment of CNV, the boric acid ester bond was broken, leading to the programmable release of PMSN-VP and $PPCeO_2$ NPs. The released VP from PMSN NPs can be targeted for uptake by the vascular endothelial cells, inhibiting YAP nuclear translocation, down-regulating angiogenic-related factors expression, and suppressing vascular endothelial cell migration and invasion. The released $PPCeO_2$ NPs exhibited ROS-scavenging and anti-inflammatory effects on BV2 cells. Importantly, our *in vivo* results demonstrated that the prepared PMSN-VP/$PPCeO_2$ NPs can effectively suppress vascular leakage and macrophage infiltration in the laser-induced CNV lesions, providing a promising therapeutic strategy for the clinical treatment of nAMD.

2. Materials and methods

2.1. Materials

3-aminopropyltriethoxysilane (APTES, 98 %), cetyltrimethylammonium chloride (CTAC, 97 %), triethanolamine (TEA, 98 %), tetraethoxysilane (TEOS, 99 %) were purchased from Sigma-Aldrich (St Louis, MO, USA). $(NH_4)_2Ce(NO_3)_6$, acetic acid (CH_3COOH), sodium acetate (CH_3COONa), and dimethyl sulfoxide (DMSO) were obtained from Aladdin (Shanghai, China). $PLGA_{5K}$-PEG_{2K}-PBA was provided by Yusi Pharmaceutical Technology Co., Ltd (Chongqing, China). The minimum essential medium (MEM) was purchased from Procell Life Science and Technology Co., Ltd (Wuhan, China). Endothelial cell medium (ECM) was purchased from ScienCell Research Laboratories (USA). Verteporfin (VP) was purchased from MedChemExpress (New Jersey, USA). Anti-CTGF (ab6992), anti-Ang2 (ab155106), anti-CD31 (ab28364), anti-F4/80 (ab6640), and antibodies were purchased from Abcam (USA). Anti-VEGF (sc-7269) antibody was purchased from Santa (USA). Anti-YAP1 (13584-1-AP) antibody was purchased from Proteintech (USA). Anti-Tubulin (AF1216) was obtained from Beyotime (China).

2.2. Synthesis of CeO_2 and $PPCeO_2$ NPs

CeO_2 NPs were prepared using a typical hydrothermal method. Briefly, $(NH_4)_2Ce(NO_3)_6$ (5 mmol) and CH_3COONa (10 g) were dissolved in 70 mL of ultrapure water, and 10 mL of CH_3COOH was then added into the solution. After stirring for 30 min, the solution was transferred to a high-pressure reactor, heated to 220 °C, and kept for 12 h. After cooling to room temperature, CeO_2 NPs were washed 4 times with DI water and lyophilized for collection. For preparing $PPCeO_2$ NPs, 5 mg CeO_2 NPs were dispersed in 5 mL of chloroform, 20 mg $PLGA_{5K}$-PEG_{2K}-PBA was dropped into the above solution, and sonicated for 5 min; chloroform was then removed by a rotary evaporation method. Afterwards, the prepared $PPCeO_2$ NPs were resuspended in pure water.

2.3. Synthesis of MSN NPs

CTAC 0.5 g (1.56 mmol) and TEA 0.04 g (0.27 mmol) were dissolved in 21.5 mL of DI water, and 1.5 mL of TEOS was added to the reaction after strong stirring at 95 °C for 1 h and then cooled down rapidly. Finally, the samples were collected by centrifugation, washed three times with ethanol, and refluxed for 3 h at 60 °C in a 0.2 % hydrochloric acid/ethanol (v/v) solution. The products were then centrifuged, washed with ethanol three times, and dried to obtain MSN NPs.

For VP encapsulation, MSN NPs and VP were dissolved in purified water at a mass ratio of 2:1 (w/w) and stirred on ice for 24 h for drug loading. Afterwards, the NPs were centrifuged and washed with pure water to remove unloaded VP. MSN-VP NPs were obtained after lyophilization. 4 mg of MSN-VP NPs was dissolved in Tris-HCl (4 mL, pH = 8.5) solution, and 2 mg of dopamine (DA) was added, stirring in the dark for 4 h at room temperature. The mixture was then centrifuged and washed with pure water to remove the unpolymerized DA, and lyophilized to obtain PMSN-VP NPs.

2.4. Synthesis of PMSN-VP@$PPCeO_2$ NPs

For preparation PMSN-VP@$PPCeO_2$ NPs, PMSN-VP NPs and $PPCeO_2$ NPs were suspended in pH 8.5 pure water and stirred for 20 h at room

temperature. After that, the precipitate was centrifuged, washed with DI water several times, and lyophilized to obtain the PMSN-VP@PPCeO$_2$ NPs.

2.5. Physicochemical characterization

The morphology of prepared NPs was acquired using a Japanese JOEL JEM-F200 field emission transmission electron microscope. Additionally, the particle size distribution of MSN and PMSN NPs was analyzed using ImageJ software. The zeta potentials of the MSN NPs, PMSN NPs, PPCeO$_2$ NPs and PMSN-VP@PPCeO$_2$ NPs were measured using a Malvern Zetasizer apparatus. The N_2 adsorption/desorption isotherms of NPs were measured on an Autosorb-iQ-MP (Quantachrome Instruments). X-ray powder diffraction (XRD) patterns were obtained by an X-ray diffraction analyzer from VG company with a scanning rate of 0.001°–8°/min and the range between 0° and 90°. The X-ray photoelectron spectroscopy (XPS) was acquired via a Thermo Scientific ESCALAB 250 Xi XPS system. The morphology of PMSN-VP@PPCeO$_2$ NPs was analyzed using scanning transmission electron microscopy (Hitachi, Japan) coupled with EDX spectroscopy. A Nicolet 6700 spectrometer (Thermo Fisher, USA) was used to measure the FTIR spectra of samples collected in the range of 4000-400 cm^{-1} with a resolution of 32 cm^{-1}. **A UV–vis spectrophotometer measured the VP concentrations in the supernatant** at 690 nm (Agilent, USA) and the drug entrapment efficiency (EE) was calculated.

2.6. In vitro VP release

VP is a hydrophobic drug, so 0.02 %–4 % (w/w) surfactants need to be added to the release medium as a solubilizer. Therefore, we use 2 mL DPBS with 0.1 % Tween-80 as the release medium. PMSN-VP@PPCeO$_2$ NPs were equally divided into three parts and placed in three EP tubes together with the release medium as parallel samples. Then, these EP tubes were placed in a constant temperature shaker at 90 rpm and 37 °C. Obtained 1 mL supernatant after centrifugation at 1 h, 2 h, 4 h, 8 h, 1 d, 2 d, 3 d, and 5 d, respectively, and the content of VP in the supernatant was determined by the UV–vis spectrophotometer. For the ROS-responsive drug release, the same method was used to determine the VP release after adding 5 mM H_2O_2 to the release medium.

2.7. In vitro cell culture

Human umbilical vein endothelial cells (HUVECs) were purchased from ScienCell (USA) and were cultured in ECM containing 5 % fetal bovine serum (FBS, ScienCell, USA), 1 % endothelial cell growth supplement (ECGS, ScienCell, USA), and 1 % penicillin/streptomycin (ScienCell, USA). The murine microglial cell line, BV2, was purchased from (Procell, China) and cultured in MEM containing 15 % FBS (Gibco, USA) and 1 % penicillin/streptomycin (Gibco, USA). All cells were cultured in a 37 °C humidified incubator under 5 % CO_2 (Thermo Scientific, USA).

2.7.1. In vitro cytotoxicities

HUVECs and BV2 cells were first seeded into 24-well plates (2×10^4/well) and incubated overnight. Then, HUVECs were treated with different concentrations of VP or PMSN-VP@PPCeO$_2$ NPs and co-cultured for 24 h, respectively. BV2 cells were treated with **varying** concentrations of PPCeO$_2$ NPs or PMSN-VP@PPCeO$_2$ NPs for 24 h, respectively. After treatment, the cells were incubated with 10 % CCK-8/culture medium in the humidified incubator for 2 h. The supernatant was then transferred the supernatant into a 96-well plate, and the absorbance at 450 nm was measured using a microplate reader (Spectramax 190, USA). Cells cultured in normal medium were used as a blank control. The relative cell viability (%) of the test groups was normalized to the value of the control group.

2.7.2. Live/dead staining

1×10^4/well HUVECs/BV2 cells were seeded into 24-well plates and incubated overnight. After co-culturing with PMSN NPs, PMSN-VP NPs, and PMSN-VP@PPCeO$_2$ NPs for 24 h, cells were stained with calcein AM reagent (live cells) and PI reagent (dead cells) using a live/dead staining kit (Invitrogen, USA), and cell morphologies were observed by the DFC7000 GT DMi8 laser scanning microscope (Leica, Germany).

2.7.3. Quantitative real-time PCR

RT-PCR was performed to determine the influence of NPs on the angiogenic response of HUVECs and the immune response of BV2. Total RNA was extracted from the cells and purified according to the user's instructions using an RNAprep pure Cell Kit (Vazyme, China). Then RNA was converted to cDNA with a HiScript III All-in-one RT SuperMix apparatus (Vazyme, China). The gene expressions were quantified using the RT-PCR System. Primers are listed in Table S1 in the Supporting Information.

2.7.4. Wound healing assay

HUVECs were seeded in 6-well plates (4×10^5 cells/well) and starved for 12 h. To find the optimum concentration, cells were scratched into one wound and cultured with the no FBS medium containing VP (2, 4 μM) or PMSN-VP@PPCeO$_2$ NPs (5, 10, 30 μg/mL), respectively. After that, in order to observe the cell migration ability of each group, photographs were taken before (0 h) and after incubation (24 h) using an inverted microscope. The cell migration capacity was analyzed using ImageJ software.

2.7.5. Transwell invasion assay

In brief, the pre-melted matrigel was diluted at 1:30 with no FBS culture medium and dropped onto the upper chamber of a transwell plate (Corning, USA). When the matrigel was solidified, HUVECs (8×10^4 cells/well) were seeded into the upper chamber and treated with different concentrations of VP or NPs. The medium in the upper chamber contained no FBS. Meanwhile, 10 % FBS/culture medium was added into the lower transwell chamber. After 24 h, gently remove the non-migrated cells on the upper side of the membrane with a cotton swab. The migrated cells on the lower side were fixed with 4 % paraformaldehyde and stained with a 0.1 % crystal violet staining solution (SangonBiotech, China). The stained cells were observed under the inverted microscope, and the number of cells was calculated using ImageJ software.

2.7.6. Tube formation assay

Briefly, each plate well was coated with matrigel and placed at 37 °C to solidify the matrigel. HUVECs were seeded into the above 24-well plate and treated with PMSN NPs, PMSN-VP NPs, and PMSN-VP@PPCeO$_2$ NPs, respectively. After 24 h of treatment, the pretreated cells were collected and seeded into 96-well plates, which had already been coated with matrigel. After 6 h of culture, tube formation was observed with an inverted microscope.

2.7.7. Fluorescence imaging of ROS scavenging

To study the cellular ROS-scavenging activity of the prepared NPs, 1×10^5 BV2 cells/well were seeded into 24-well plates. After 24 h, remove the culture medium and replace it with fresh culture medium containing different concentrations of PPCeO$_2$ NPs (5, 50, 100 μg/mL) and PMSN-VP@PPCeO$_2$ NPs (5, 10, 30 μg/mL). Following 24 h of exposure, the cells were washed twice and cultured with 400 μM of H_2O_2 for 4 h prior to the addition of DCFH-DA (1:1000, Phygene, China). Wash off the excess probe after 30 min of DCFH-DA treatment. Finally, the intracellular ROS levels were visualized under a DMi8 microscope. **The same procedure was performed f**or the ROS scavenging activity of PMSN NPs, PMSN-VP NPs, and PMSN-VP@PPCeO$_2$ NPs.

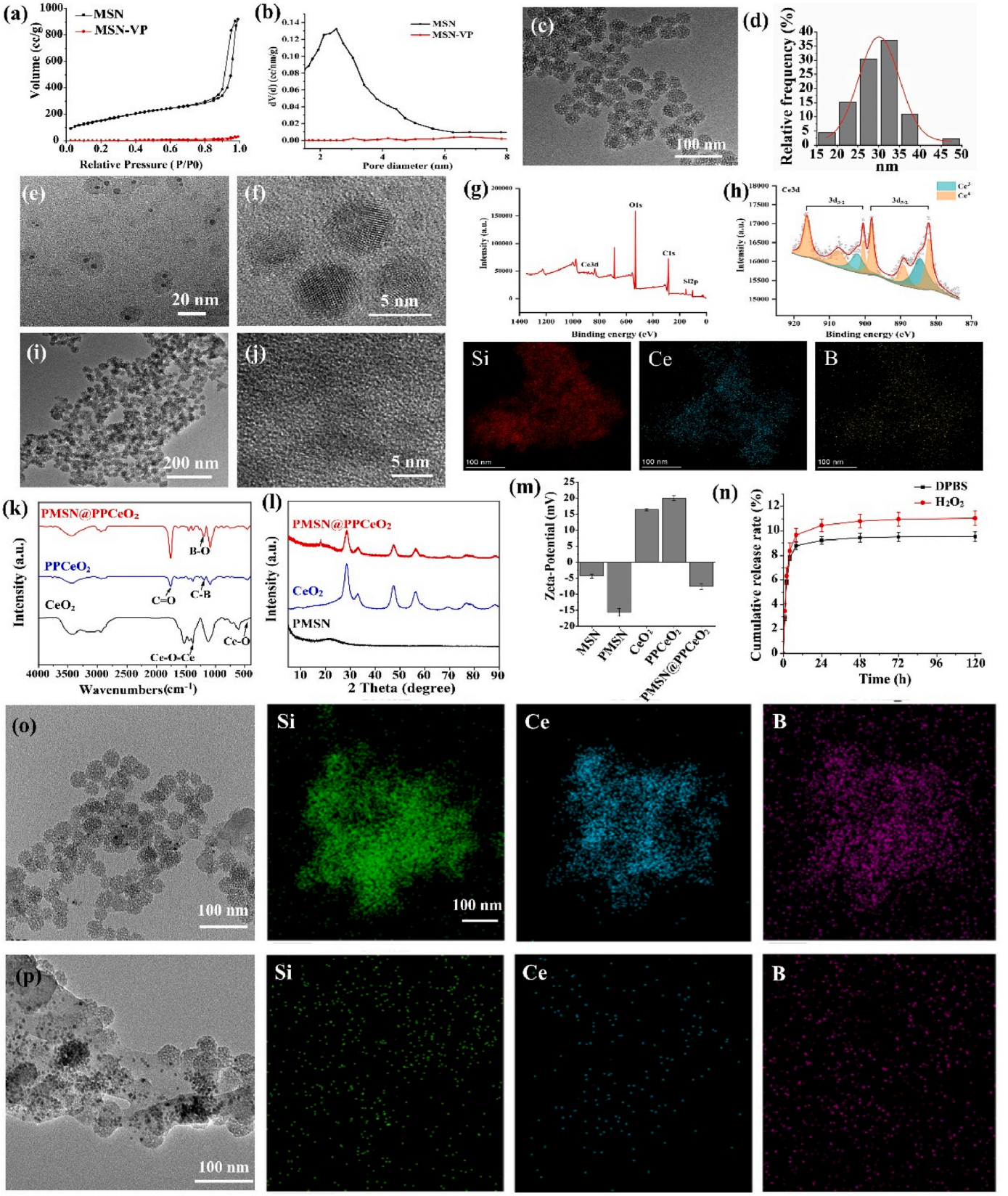

Fig. 1. Characterizations of as-fabricated NPs. (a) N_2 adsorption-desorption isotherms of the MSN and MSN-VP NPs; (b) Pore size distribution of MSN and MSN-VP NPs; (c) TEM images and (d) size distribution of PMSN NPs; (e) TEM and (f) HRTEM images of $PPCeO_2$ NPs; (g) Survey XPS spectra of $PPCeO_2$; (h) High-resolution XPS spectra of Ce 3d in CeO_2; (i) TEM and (j) HRTEM images of PMSN@$PPCeO_2$ NPs, and mapping images of Si, Ce and B presented in PMSN@$PPCeO_2$ NPs; (k) FTIR spectra of CeO_2, $PPCeO_2$ and PMSN@$PPCeO_2$ NPs; (l) XRD patterns of PMSN, CeO_2 and PMSN@$PPCeO_2$ NPs; (m) Zeta potential of MSN, PMSN, CeO_2, $PPCeO_2$, and PMSN@$PPCeO_2$ NPs; (n) In vitro release of VP from PMSN-VP NPs in both DPBS and H_2O_2 solutions; TEM and mapping images of Si, Ce and B presented in PMSN@$PPCeO_2$ NPs after treating in (o) DPBS and (p) H_2O_2 conditions for 24 h.

2.7.8. Flow cytometric measurement of ROS

The experimental groups were the same as the measurements of ROS levels. 2×10^5 BV2 cells/well were seeded in 6-well plates. Then different NPs were incubated with BV2 cells for 24 h. Lipopolysaccharide (LPS, 200 ng/mL) was used to induce oxidative *stress and was treated for 4 h.* Afterwards, the cells were washed and cultured with DCFH-DA diluent for 30 min. The cell suspension was washed twice with PBS and centrifuged at 1000 rpm for 4 min. The detection was immediately performed on the C6 Plus Flow Cytometer (BD C6 Plus, USA).

2.7.9. Western blot analysis

Total proteins from treated cells were harvested using a RIPA lysis buffer (Thermo Scientific, USA) containing a 1 % protease and phosphatase inhibitor cocktail, and the extracted proteins were sonicated, fully rupturing the cells. Protein concentration was determined using a BCA protein assay kit (Thermo Scientific, USA). Equal amounts of lysate (30 μg) were added to 10 % SDS–PAGE gels (Epizyme, China), then transferred to PVDF membranes (Epizyme, China) and blocked in 5 wt% milk for 1 h. The membranes were incubated in primary antibody solutions (anti-CTGF, 1:500; anti-Ang2, 1:1000; anti-Tubulin, 1:1000) at 4 °C overnight and then probed with horseradish peroxidase (HRP)-conjugated secondary antibodies. Protein signaling was visualized using the ChemiDoc XRS + Imager (Bio-Rad Laboratories Inc, USA).

2.7.10. Immunofluorescence

For the immunofluorescence staining, 5×10^4 HUVEC cells/well were cultured in 24-well plates, and the same treatment was carried out. After culturing for 24 h, cells were washed with DPBS and fixed with 4 % paraformaldehyde for 10 min at RT. After that, they were permeabilized with 0.1 % Triton X-100 (Beyotime, China) for 5 min and blocked with 1 % BSA (Beyotime, China) for 20 min. The primary antibody (anti-YAP1, 1:200) was diluted and incubated with the cells at 4 °C overnight. The cells were then washed gently with DPBS and treated with the secondary antibody Alexa Fluor 488 goat antirabbit IgG (H + L) antibody (1:200, Invitrogen) for 1 h and protecting from light. Finally, after the washing period, nuclei were counter-stained with **a** mounting medium containing DAPI and stored at 4 °C. Images of these cells were then obtained using a Zeiss LSM880 confocal laser scanning microscope.

2.7.11. In vivo laser-induced mouse CNV model

Animal care and surgery procedures followed the protocol approved by the Use Committee of Wenzhou Medical University (China). Mice (C57BL/6J, 6–8 weeks, male) weighing 18–20 g were obtained from the Zhejiang Provincial Laboratory Animal Center. The laser-induced CNV models were constructed as in previous studies with minor modifications [32]. Briefly, C57BL/6J mice were first anesthetized, and their pupils were dilated with 1 % tropicamide. After dilation of the pupils, four photocoagulated spots were generated at approximately equal distances from the optic nerve using a Micron IV retinal image-guided laser system (Phoenix Research Labs, Pleasanton, CA, USA). The applied laser parameters were a duration of 100 ms, 200 mW power, and a spot size of 50 μm. The day of molding was taken as day 0, and the drugs (Conbercept 10 mg/mL, PMSN NPs, PMSN-VP NPs, PMSN-VP@PPCeO$_2$ NPs) were administered by intravitreal injection on day 1, the dosing volume per eye was 2 μL. On days 7 and 14, fundus images were captured after intraperitoneal injection of fluorescein sodium (0.1 mL/10 g, 4 %) and the area of the CNV lesion was quantified using ImageJ software.

2.7.12. Retinal/choroidal flat mounts, immunofluorescence, and H&E staining

Briefly, eyes from CNV mice were quickly removed. The eyeball was dehydrated, embedded in paraffin and cut into slices. Some of the specimens were stained with H&E staining, while the others were co-incubated with the primary antibody at 4 °C overnight and stained with secondary antibodies. Photographs of the tissue slices were taken with a DM750 microscope (Leica, Germany). ImageJ was used to analyze the area of new blood vessels.

2.7.13. Biosafety analysis

After 14 days of treatment, mice were euthanized, and their whole blood and serum were collected for hematology and blood biochemistry analysis. Major organs were collected, fixed in 4 % formalin, embedded in paraffin, sectioned, and stained with H&E. Photographs of the tissue slices were taken with an inverted microscope.

2.7.13.1. Statistical analysis. All data expressed were presented as the mean ± standard deviation. Statistical analysis was performed using the Origin and GraphPad Prism software. A two-tailed unpaired Student's t-test was used to compare two groups, and a one-way analysis of variance was used to compare multiple groups. The threshold of $P < 0.05$ was determined as statistical significance.

3. Results and discussion

3.1. Synthesis and characterization of nanoparticles

To achieve the anti-VEGF and ROS-scavenging properties, here, an MSN-Ceria nanocomposite was developed. Firstly, VP was encapsulated into a polydopamine (PDA) coated mesoporous silica nanoparticle (PMSN). The TEM image showed the uniform MSN exhibited spherical and porous structures with an average diameter of 32.6 ± 0.2 nm (Fig. S1). After VP encapsulation, the surface area of MSN was decreased from 603.78 m^2g^{-1} to 49.43 m^2g^{-1}, and the pore volume was reduced from 1.37 cc/g nm to 0.07 cc/g (Fig. 1a and b). After that, the surface of MSN-VP NPs was functionalized with PDA through an *in situ* polymerization of dopamine. The bending vibration peak of -OH in Ar-OH (1388 cm^{-1}) and the C=C vibration peak in the benzene ring skeleton (1500 cm^{-1}) were detected in PMSN NPs, indicating the successful PDA surface modification (Fig. S2). The ceria quantum dot with a diameter of around 4.2 ± 0.5 nm and **apparent** lattice structure was synthesized by a hydrothermal method (Fig. S3). The ceria quantum dot was then decorated with a cationic liposome, $PLGA_{5K}$-PEG_{2K}-PBA (PP), to create a cerium oxide liposome composite (PPCeO$_2$). Our TEM image confirmed the PP decoration since the diameter of the ceria was slightly increased, and an **apparent** spherical liposome structure was observed on the surface of PPCeO$_2$ NPs (Fig. 1e and f). The ROS-scavenging capacity of ceria was due to the co-existence of Ce^{3+} and Ce^{4+} that can reversibly bind to oxygen [33]. X-ray photoelectron spectroscopy (XPS) spectra further verified the chemical composition and the Ce^{3+}/Ce^{4+} ratio. In the XPS spectra, the peaks of Ce^{3+} in CeO$_2$ appeared at 884.2 and 902.5 eV, and the peaks of Ce^{4+} were shown at 881.9, 888.3, 897.8, 900.4, 907.2 and 916.2 eV with a surface Ce^{3+}/Ce^{4+} ratio of 20.49 % (Fig. S4). In the PPCeO$_2$ NPs, a slight shift of the characteristic peaks of Ce^{3+} (884.6 and 902.3 eV) and Ce^{4+} (882.1, 889.2, 898.1, 900.5, 907.6 and 916.4 eV) was observed compared to that of CeO$_2$ NPs (Fig. 1g and h). Most importantly, the Ce^{3+}/Ce^{4+} ratio in PPCeO$_2$ NPs was increased to 50.15 % compared to 20.49 % in CeO$_2$ NPs, indicating the improved ROS-scavenging ability.

The PMSN NPs were further combined with PPCeO$_2$ NPs through borate ester bonds between the phenylboronic acid group from PP and phenolic hydroxyl groups of PDA. The TEM image of PMSN@PPCeO$_2$ NPs exhibited a uniform spherical structure, and a CeO$_2$ lattice structure was observed on the surface of PMSN NPs (Fig. 1i and j). Additionally, the Si, Ce, and B elements were detected on the PMSN@ PPCeO$_2$ NPs TEM elemental mapping images, which were derived from PMSN, CeO$_2$ and PP, indicating the successful binding of PMSN and PPCeO$_2$ NPs. The FTIR spectra showed the characteristic peaks around 458 and 1388 cm^{-1} in CeO$_2$, which belonged to the stretching vibration peak of Ce-O-Ce. In the PPCeO$_2$ NPs, new peaks around 1195 cm^{-1} and 1760 cm^{-1} were detected, which were attributed to the C-B and C=O in PP, and also

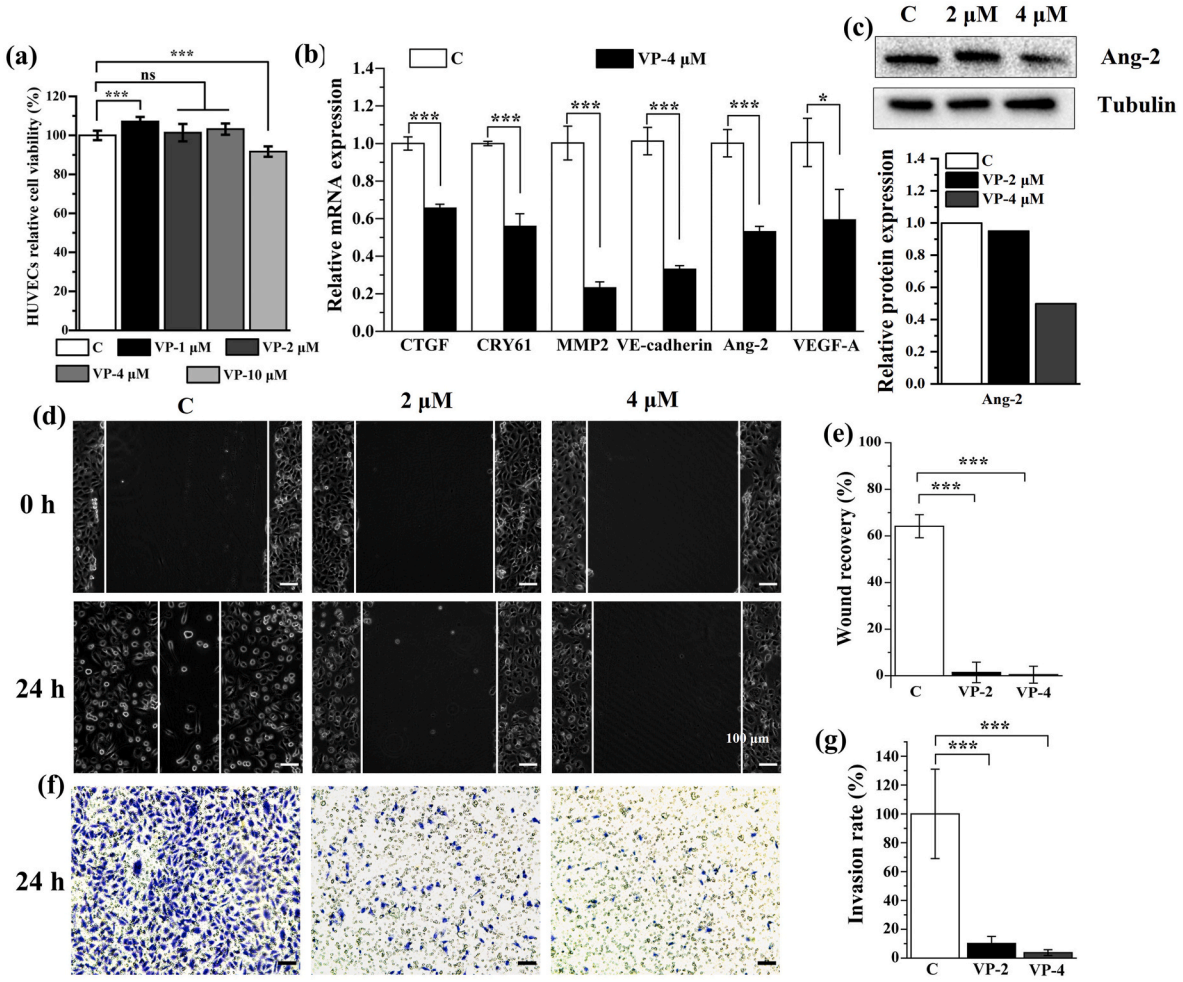

Fig. 2. Anti-angiogenic activities of VP. (a) Relative cell viabilities of different concentrations of VP on HUVECs; (b) CTGF, CRY61, MMP2, VE-cadherin, Ang-2 and VEGF-A gene expressions in HUVECs after cultured in VP (4 μM) for 1 day; (c) Western blot and quantification analysis of the Ang-2 protein expression in HUVECs after treated with VP (2 μM, 4 μM); (d) Representative bright-field images of the scratch migration assay of HUVECs in VP (2 μM, 4 μM); (e) Quantification of the scratch migration; (f) Transwell invasion of HUVECs in VP (2 μM, 4 μM) and (g) Quantification of the cell invasion. Data are expressed as mean ± SD ($n = 3$) (*$p <$ 0.05, ***$p < 0.001$).

indicated the successful decoration of PP on the surface of CeO_2 NPs. Moreover, the B-O chemical bond (1385 cm^{-1}) was formed after the mixing of PMSN and $PPCeO_2$ NPs, which was attributed to the borate ester bonds (Fig. 1k). The XRD patterns of PMSN showed a broad peak around 22°, and the CeO_2 NPs showed a cubic fluorite structure. After the combination of PMSN and CeO_2 NPs, the intensity of sharp diffraction peaks of the CeO_2 decreased and the peak width increased (Fig. 1l). The MSN showed a negative charge with a potential of −4.3 mV, and the potential was further decreased after PDA coating (PMSN, −15.6 mV). The zeta potential of CeO_2 NPs was 16.4 mV; after being modified with PP, the zeta potential of $PPCeO_2$ NPs slightly increased to 20 mV. When the PMSN NPs were mixed with $PPCeO_2$ NPs, the hybrid NPs showed a potential of −7.5 mV, confirming the surface modification of $PPCeO_2$ NPs onto the PMSN NPs (Fig. 1m).

The ROS-responsive release behavior of PMSN-VP@$PPCeO_2$ NPs was carried out in DPBS and hydrogen peroxide (H_2O_2) solutions, respectively. Our data revealed that a higher amount of VP was released in H_2O_2 compared to the DPBS condition over a period of 120 h (Fig. 1n). We further used the TEM to observe the morphologies of PMSN-VP@$PPCeO_2$ NPs after treatment in DPBS and H_2O_2 solutions for 24 h. The TEM images showed that the structural integrity of PMSN-VP@$PPCeO_2$ NPs was maintained in DPBS solution (Fig. 1o), whereas in the H_2O_2 condition, partially degraded PMSN NPs and $PPCeO_2$ NPs were released from PMSN-VP NPs (Fig. 1p). All these results confirmed the ROS-responsive properties of PMSN-VP@$PPCeO_2$ NPs.

3.2. *Biological functions of VP*

Verteporfin (VP), a benzoporphyrin derivative, is usually used as a photosensitizer in photodynamic therapy for AMD. Additionally, VP is also an inhibitor of the YAP/TEAD complex, thereby regulating angiogenic-related and cell migration gene expression [16,17,19,34,35]. The *in vitro* cytotoxicities of native VP were carried out in the HUVECs using the CCK8 assay. As shown in Fig. 2a, significant cytotoxicity was observed when the VP concentration reached 10 μM after 24 h of culture. Our RT-PCR data showed that VP (4 μM) inhibited the gene expression of CTGF, CRY61, MMP2, Ang-2, and VEGF-A, which are related to angiogenesis and subretinal fibrosis. Subretinal fibrosis is the final stage of nAMD, and CTGF has been reported to influence extracellular matrix (ECM) formation, angiogenesis, and the fibrosis processes [36]. MMP2 acts as the activator of TGF-β, which is an essential mediator of fibrosis through the PI3K/AKT/ERK signaling pathway [37]. Our western blot analysis also confirmed that VP (4 μM) markedly suppressed Ang-2 protein expression. To further investigate the anti-angiogenic effects of VP, wound healing assays and cell invasion tests were carried out. The migratory capacity of HUVECs was restrained after treatment with VP at both 2 μM and 4 μM concentrations (Fig. 2d and e). Similar results were also supported by the cell invasion data

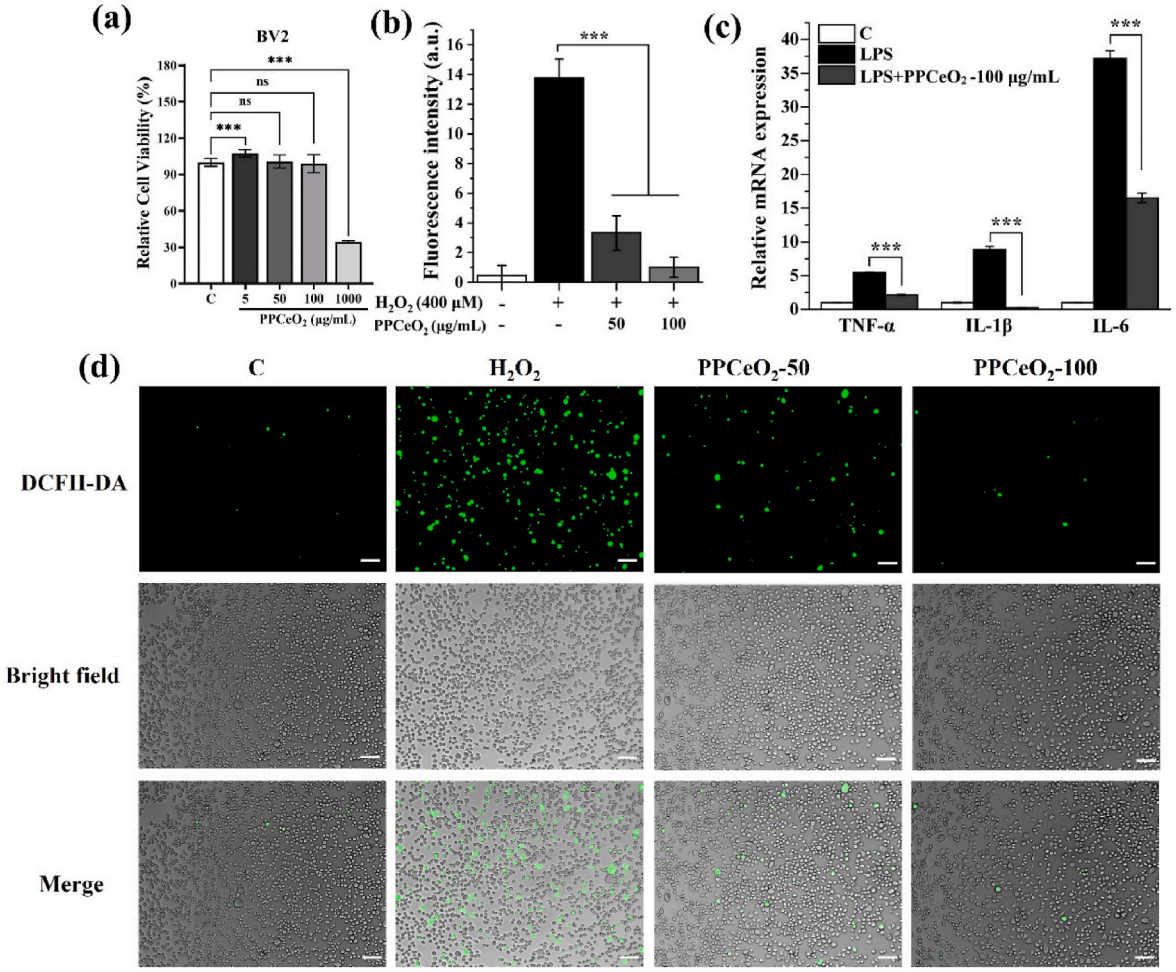

Fig. 3. ROS-scavenging and anti-inflammatory activities of $PPCeO_2$ NPs. (a) Relative cell viabilities of different concentrations of $PPCeO_2$ NPs in BV2 cells for 1 day; (b) Quantification of the fluorescence staining; (c) The relative gene expression levels (TNF-α, IL-1β and IL-6) of BV2 cells treated with LPS and LPS + $PPCeO_2$-100 μg/mL for 1 day; (d) ROS level (DCFH-DA staining), bright field and merge images of BV2 cells exposed to Control, H_2O_2, H_2O_2+$PPCeO_2$-50 μg/mL and H_2O_2+$PPCeO_2$-100 μg/mL. Data are expressed as mean ± SD ($n = 3$) (***$p < 0.001$).

(Fig. 2f and g). These observations suggested that VP exhibited anti-angiogenic and subretinal fibrosis effects in HUVECs *in vitro*. Based on the above results, we chose VP (4 μM) for the subsequent study.

3.3. Biocompatibility, ROS-scavenging, and anti-inflammatory capacities of $PPCeO_2$ NPs

In addition to neovascularization, oxidative stress and inflammation are also key trigger factors in the pathological process of AMD [5,38]. Here, the anti-oxidative and anti-inflammatory capacities of $PPCeO_2$ NPs were assessed on BV2 cells. According to the CCK8 data, obvious cell toxicity was detected when the applied concentration was 1000 μg/mL after culturing for 24 h (Fig. 3d). Here, H_2O_2 (400 μM) was used to stimulate oxidative stress in BV2 cells. Our fluorescence staining data showed that $PPCeO_2$ NPs exhibited remarkable DCFH-DA scavenging efficiency in a dose-dependent manner (Fig. 3b–e), indicating that $PPCeO_2$ NPs had excellent antioxidant activity. Additionally, lipopolysaccharide (LPS) was used to induce the pro-inflammatory response in BV2 cells. After co-culture with BV2 cells for 24 h, $PPCeO_2$ NPs (100 μg/mL) markedly decreased M1-related gene expression (TNF-α, IL-1β, and IL-6), showing the excellent anti-inflammatory effects of $PPCeO_2$ NPs. All these results suggested that the prepared $PPCeO_2$ NPs had excellent ROS-scavenging and anti-inflammatory capacities in microglia and could be used to modulate the immune microenvironment in the CNV lesions.

3.4. In vitro ROS-scavenging and anti-inflammatory capacities of PMSN-VP@$PPCeO_2$ NPs

The PMSN-VP@$PPCeO_2$ NPs were formed through the borate ester bonds between the phenylboronic acid group of PP and phenolic hydroxyl groups of PDA. To study the influence of PMSN-VP@$PPCeO_2$ NPs concentrations (5, 10, 30, 50 and 100 μg/mL) on the cytotoxicities of HUVECs, BV2, and ARPE-19 cells, a CCK8 assay was carried out (Fig. S5). Lower cell viability in HUVECs was measured when the PMSN-VP@$PPCeO_2$ NPs concentration reached up to 100 μg/mL for 1 day. **At the same time,** considerable cytotoxicity of PMSN-VP@$PPCeO_2$ NPs on BV2 cells was noticeable even when the concentration was at 30 μg/mL after culturing for 1 day, with relative cell viability around 86.6 %. While on the ARPE-19 cells, obvious cytotoxicity was detected when the PMSN-VP@$PPCeO_2$ NPs concentration was at 10 μg/mL, with relative cell viability around 81.5 %. Moreover, the DCFH-DA staining data revealed that PMSN-VP@$PPCeO_2$ (5, 10 μg/mL) showed significant ROS scavenging effects, while the concentration of 30 μg/mL had no such effect (Fig. S6). Our RT-PCR data showed that PMSN-VP@$PPCeO_2$ (10 μg/mL) had the strongest anti-angiogenic effects on HUVECs (Fig. S7). According to the above results, the concentration of 10 μg/mL PMSN-VP@$PPCeO_2$ NPs was chosen as the optimal concentration and used in the subsequent experiments.

The cytotoxicities of PMSN, PMSN-VP and PMSN-VP@ $PPCeO_2$ NPs on BV2 cells showed that no obvious cell toxicities were detected in all

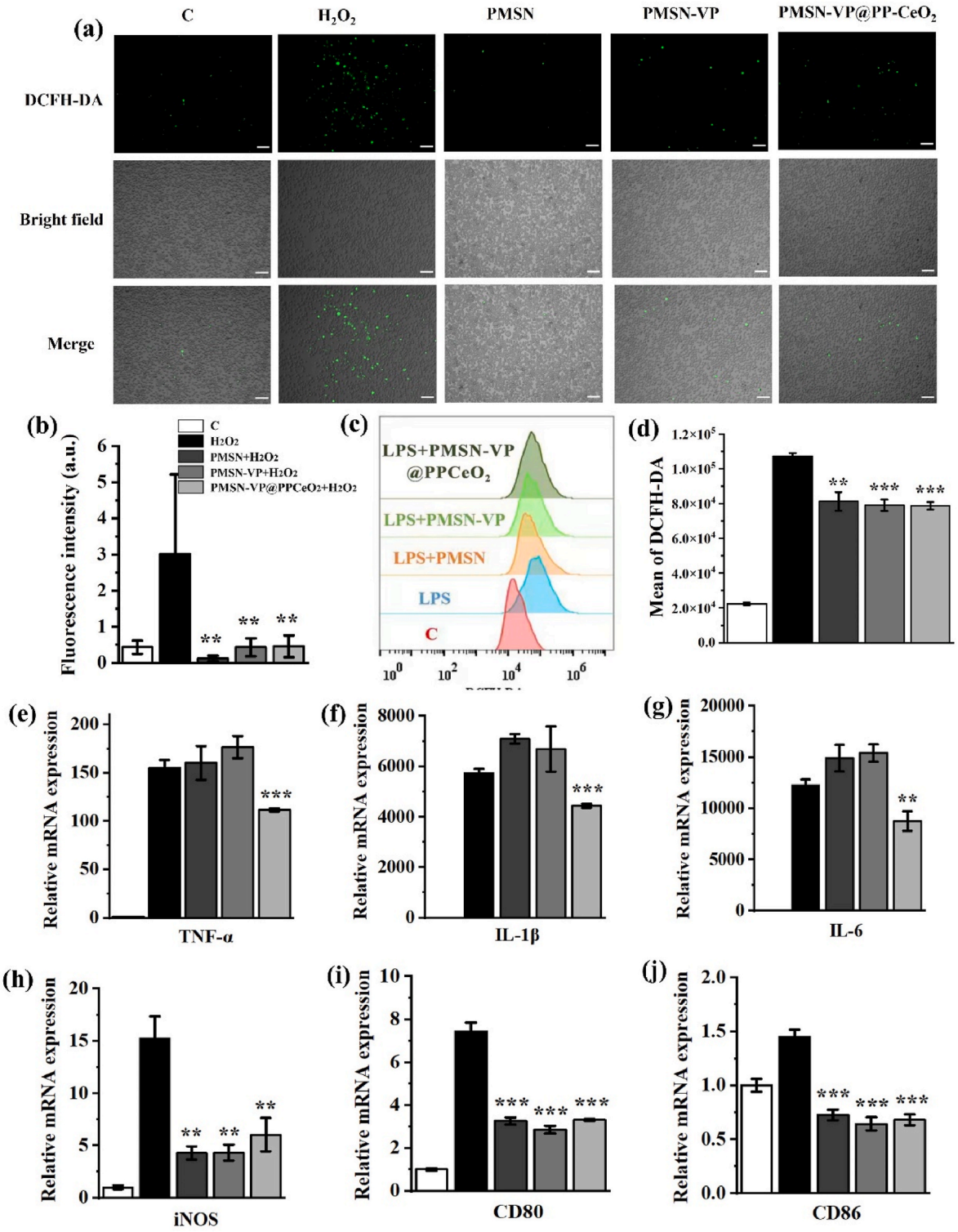

Fig. 4. ROS-scavenging and anti-inflammatory abilities of NPs. (a) DCFH-DA staining, bright field and merge pictures of BV2 cells cultured on Control, H_2O_2, PMSN + H_2O_2, PMSN-VP + H_2O_2, PMSN-VP@PPCeO$_2$+H_2O_2 (Scale bar = 200 μm); (b) Quantification of the fluorescence staining; (c) Representative flow cytometry analysis of ROS levels in BV2 cells; (d) Quantification of flow cytometry data; The relative gene expression levels of (e) TNF-α; (f) IL-1β; (g) IL-6; (h) iNOS; (i) CD80 and (j) CD86 of BV2 cells cultured on different groups. Data are expressed as mean ± SD ($n = 3$) (**$p < 0.01$, ***$p < 0.001$).

three types of NPs (Fig. S8). Similar results were also observed in the live/dead staining of BV2 cells in each group of NPs after 24 h of treatment. The accumulation of ROS in CNV sites leads to tissue damage and overexpression of inflammatory cytokines; here, the ROS-scavenging ability of each group was evaluated in BV2 cells. Our data showed that a reduction in oxidative stress was achieved after the treatment of PMSN, PMSN-VP, and PMSN-VP@PPCeO$_2$ NPs (Fig. 4a–e). These results were supported by the flow cytometry data (Fig. 4g and h). Moreover, the anti-inflammatory effects of PMSN-VP@PPCeO$_2$ NPs were also investigated. These encouraging data suggested that the

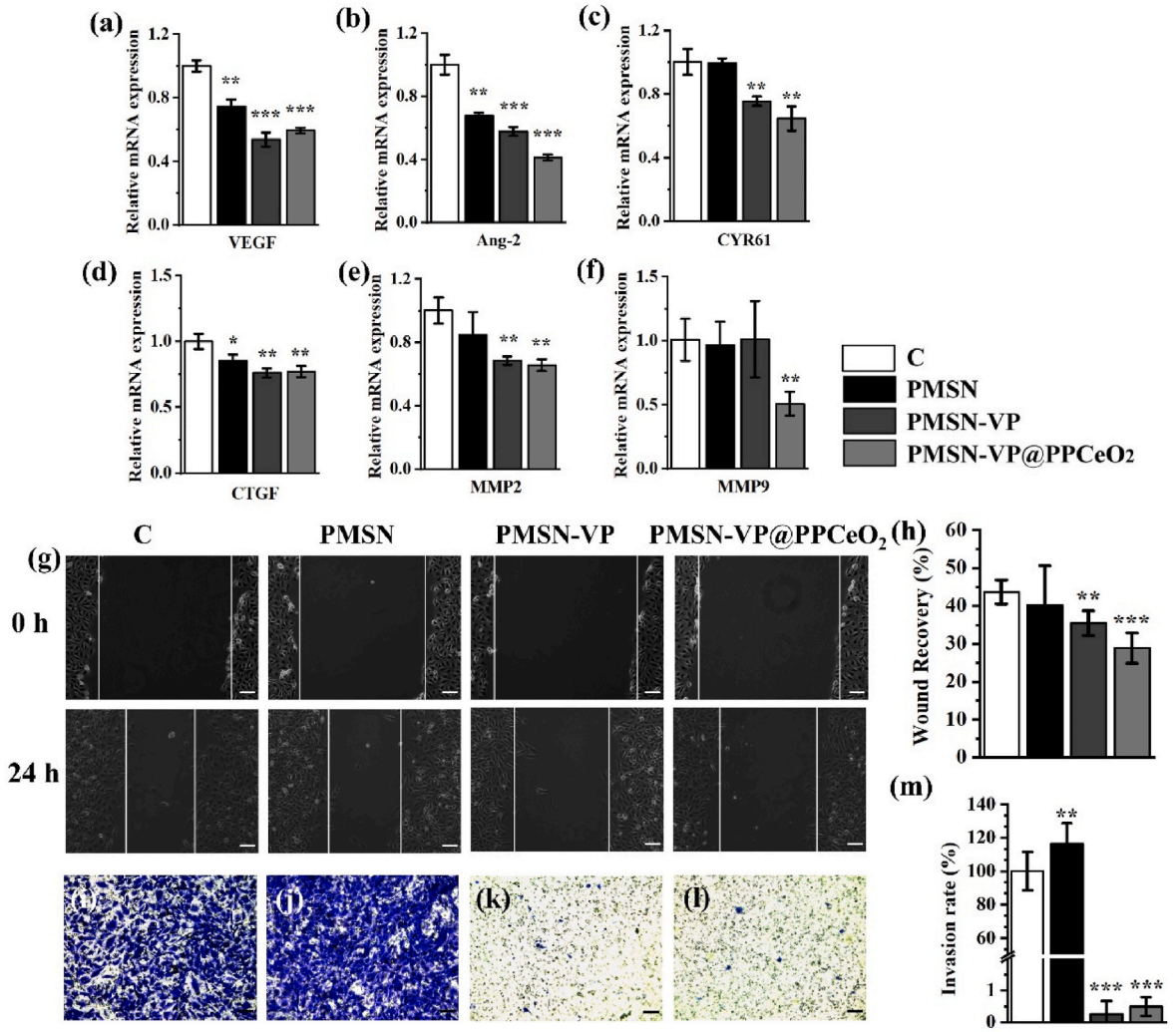

Fig. 5. ***In vitro*** **anti-angiogenic activity of PMSN-VP@PPCeO$_2$ NPs.** The relative gene expression of (a) VEGF; (b) Ang-2; (c) CYR61; (d) CTGF; (e) MMP2; (f) MMP9 in HUVECs after the treatment of PMSN, PMSN-VP and PMSN-VP@PPCeO$_2$ NPs; (g) Representative bright-field images of the scratch migration assay of HUVECs in different groups; (h) Quantification of wound healing data; Transwell invasion of HUVECs in (i) Control; (j) PMSN; (k) PMSN-VP; (l) PMSN-VP@PPCeO$_2$ NPs; (m) Quantification of the cell invasion data. Data are expressed as mean ± SD ($n = 3$) ($^*p < 0.05$, $^{**}p < 0.01$, $^{***}p < 0.001$).

PMSN-VP@PPCeO$_2$ NPs significantly down-regulate LPS-induced M1 phenotype gene markers (TNF-α, IL-1β, IL-6, iNOS, CD80, and CD86) expression after 1 day of treatment (Fig. 4i–n). It is worth noting that PMSN and PMSN-VP can only decrease pro-inflammatory factors (iNOS, CD80, and CD86) expression (Fig. 4l–n), which may be attributed to the polydopamine (PDA) on the surface of MSN. Overall, PDA and CeO$_2$ together contribute to the anti-inflammatory effects of PMSN-VP@PPCeO$_2$ NPs.

3.5. *In vitro anti-angiogenic effects of PMSN-VP@PPCeO$_2$ NPs*

To further explore the anti-angiogenic activities of prepared NPs, RT-PCR, wound healing assay, transwell invasion assay and tube formation tests were carried out on HUVECs. Cell toxicities revealed that lower cell viabilities were observed on PMSN-VP and PMSN-VP@PP-CeO$_2$ NPs, with the cell viability around 93.1 % and 90.4 %, respectively (Fig. S9). Our RT-PCR data revealed that PMSN-VP@PPCeO$_2$ NPs distinctly inhibited pro-angiogenic genes (VEGF, Ang-2, CYR61, CTGF, MMP2, and MMP9) expression in HUVECs, and PMSN-VP NPs decreased CYR61, CTGF, Ang-2, VEGF, and MMP2 expression. However, the PMSN-VP@PPCeO$_2$ NPs showed a better inhibitory effect (Fig. 5a–f). It was worth noting that PMSN alone downregulated CTGF, Ang-2, and VEGF expression in HUVECs compared to the control group. The cell migration data showed that both PMSN-VP and PMSN-VP@PPCeO$_2$ NPs decreased HUVEC migration compared to the control group, whereas PMSN NPs did not have this effect after 24 h of treatment (Fig. 5g and h). Moreover, the HUVEC transwell invasion was significantly inhibited when HUVECs were treated with PMSN-VP and PMSN-VP@PPCeO$_2$ NPs (Fig. 5i–m). The tube formation assay is also a widely used test *in vitro* to evaluate the angiogenic ability of HUVECs [39]. Here, capillary-like networks were formed on HUVECs after 24 h of culture (Fig. S10), with fewer capillary-like tubes observed in the PMSN-VP and PMSN-VP@PPCeO$_2$ groups. Quantitative analysis confirmed reductions in the total branch length, number of meshes, and number of junctions per field in these groups. All these results demonstrated that the anti-angiogenic properties of PMSN-VP@PPCeO$_2$ NPs were primarily attributed to VP, while the antioxidant properties of PPCeO$_2$ NPs endowed synergistically to the anti-angiogenesis activity in HUVECs.

3.6. *The protective effect of PMSN-VP@PPCeO$_2$ NPs in the laser-induced mouse CNV model*

To evaluate the therapeutic effect of PMSN-VP@PPCeO$_2$ NPs in nAMD, intravenous injection of Conbercept, PMSN, PMSN-VP, and PMSN-VP@PPCeO$_2$ NPs in a laser-induced CNV model was performed. A schematic illustration of the CNV model establishment and treatment

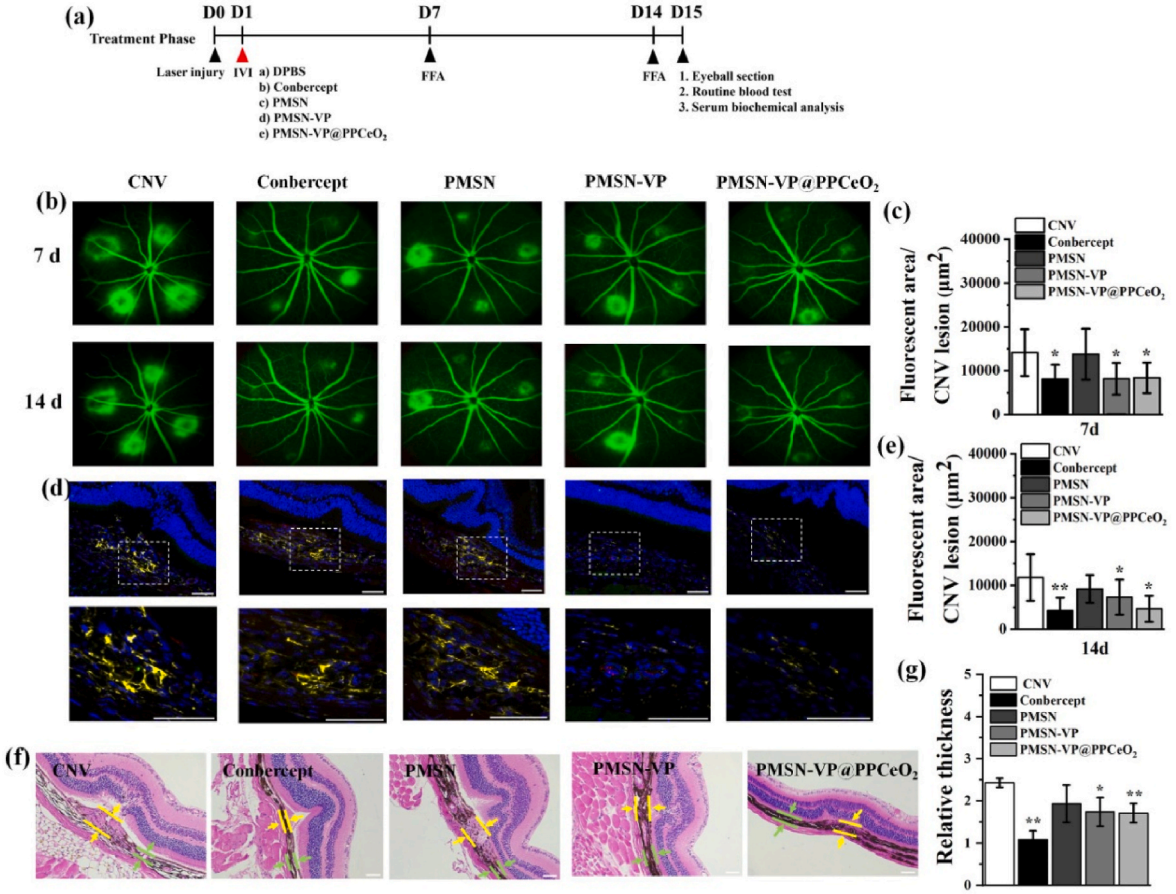

Fig. 6. Therapeutic efficacy of the NPs on the laser-induced mouse CNV model. (a) Diagram of schedule of experimental workflow; (b) Representative fundus photographs of CNV regions after treated with different groups for 7 days and 14 days; Quantification of CNV lesion areas of each group after (c) 7 days and (e) 14 days of treatment; (d) F4/80 immunofluorescence staining of each group in CNV lesion areas (F4/80: yellow, DAPI: blue); (f) Histological H&E analysis of the CNV after 14 days of treatment; (g) Quantification of the thickness of the lesion area based on the H&E staining images. (For interpretation of the references to colour in this figure legend, the reader is referred to the Web version of this article.)

process with different groups is shown in Fig. 6a. Severe vascular leakage in the neovascular lesions was observed, confirming that the laser-induced CNV model was successfully constructed (Fig. 6b). The FFA images showed that the Conbercept, PMSN-VP and PMSN-VP@PPCeO$_2$ groups markedly alleviated vascular leakage from CNV lesions compared to the saline group after 7 days of treatment (Fig. 6b and c). Additionally, the CNV lesion areas were further reduced in the Conbercept, PMSN-VP and PMSN-VP@PPCeO$_2$ groups after 14 days of treatment (Fig. 6e). It was worth noting that the effects of PMSN-VP and PMSN-VP@PPCeO$_2$ NPs on vascular leakage inhibition were similar after 7 days of treatment, while the PMSN-VP@PPCeO$_2$ NPs showed a better inhibitory effect compared to PMSN-VP NPs after 14 days of treatment. Consistent with FFA results, eyes treated with **PMSN-VP@PPCeO2 NPs** exhibited the smallest remaining CNV area (Fig. S11). Importantly, immunofluorescence staining of F4/80 (green/yellow) and DAPI (blue) is presented in Fig. 6d. Quantitative analysis revealed a significant increase in F4/80+ macrophages within CNV lesions 14 days post-laser photocoagulation. However, both PMSN-VP and PMSN-VP@PPCeO$_2$ treatment groups showed a dramatic reduction in F4/80+ cell infiltration compared to the control. Additionally, immunofluorescence staining for CD31, 4-Hydroxy-2-nonenal (HNE-2), IL-1β, and iNOS revealed that the PMSN-VP@PPCeO2 group had significantly lower levels of HNE-2, IL-1β, and iNOS compared to the other groups 14 days after laser photocoagulation (Fig. S12). Meanwhile, the Conbercept, PMSN-VP, and PMSN-VP@PPCeO2 groups all showed reduced CD31 levels (Fig. S13). These data suggested that the anti-angiogenic activity of VP played the leading role in reducing vascular leakage in CNV lesions, and the antioxidant and anti-inflammatory effects of PPCeO$_2$ also suppressed CNV lesions. Moreover, our H&E staining data showed that the maximum CNV thickness was significantly reduced in the Conbercept, PMSN-VP and PMSN-VP@PPCeO$_2$ groups. Visual impairment caused by CNV is not only due to choroidal vascular dysfunction; oxidative stress and inflammation are also involved in CNV growth [40,41]. Elevated ROS levels will cause damage to proteins, lipids, and mitochondrial DNA, ultimately leading to RPE cell death [5,42]. Additionally, inflammatory factors such as interleukin-6 (IL-6) and interleukin-8 (IL-8) will also promote the progression of CNV [43]. Therefore, the combinational therapeutic strategy with a combined reduction of ROS, inflammatory factors, and angiogenesis is essential for efficiently treating CNV. Finally, the biosafety of the prepared NPs was systematically studied through the H&E staining of the main organs (Fig. S14), blood biochemistry analysis (Fig. S15) and flash electroretinography (fERG, Fig. S16). No **noticeable** histopathological changes in the main organs (heart, liver, spleen, lung, and kidney) were observed after intravenous treatment with Conbercept, PMSN, PMSN-VP, and PMSN-VP@PPCeO$_2$ NPs for 14 days. Our blood routine (WBC and lymph) and hepatic and renal function indexes such as aspartate aminotransferase (AST), alanine aminotransferase (ALT), urea, and creatinine (CREA) results revealed that no significant differences were detected between the treated groups and the saline group. Moreover, fERG data revealed that 7 days post-injury, the amplitude of the a and b waves in the CNV group was significantly reduced compared to the healthy group. In contrast, the retinal function of mice treated with PMSN and PMSN-VP NPs showed improvement, with the therapeutic

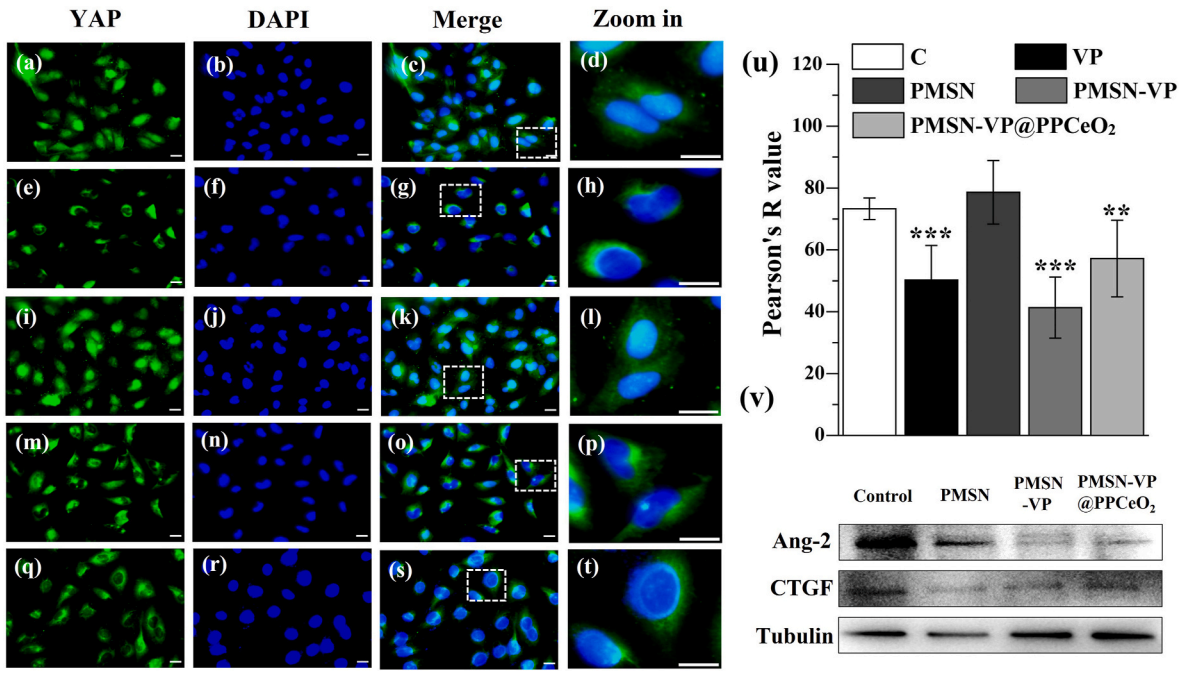

Fig. 7. VP-contained NPs inhibited nuclear translocation of YAP. Immunofluorescence images of YAP (green) and nuclei (DAPI, blue) in HUVECs after treated with (a–d) Control, (e–h) VP, (i–l) PMSN, (m–p) PMSN-VP and (q–t) PMSN-VP@PPCeO$_2$ NPs; (d, h, l, p, t) Confocal microscopy analysis of YAP colocalization with DAPI in HUVECs of each group; (u) Quantification of the Pearson Correlation Coefficient of each group; (v) Western blot analysis of the Ang-2, CTGF and Tubulin expression in HUVECs. Data are expressed as mean ± SD ($n = 3$) (**$p < 0.01$, ***$p < 0.001$). (For interpretation of the references to colour in this figure legend, the reader is referred to the Web version of this article.)

effect of PMSN-VP@PPCeO$_2$ comparable to that of Conbercept group. After 14 days of treatment, there was a significant increase in the amplitudes of both a and b waves. These results indicate that PMSN-VP@PPCeO$_2$ NPs effectively alleviates retinal dysfunction caused by CNV.

3.7. The mechanism underlying PMSN-VP@PPCeO$_2$ NPs therapy

YAP is the major effector of the Hippo pathway that regulates vascular sprouting, remodeling, and vascular barrier formation [12,13]. Here, the HUVECs were treated with different groups of materials, and our confocal images revealed that neat VP can inhibit the nuclear translocation of YAP in HUVECs, and VP-containing NPs (PMSN-VP and PMSN-VP@PPCeO$_2$) maintained this function. This was also confirmed by the quantification of Pearson's value (Fig. 7v) that both VP and VP-containing NPs prevented the nuclear translocation of YAP. Moreover, our western blot data showed that CTGF and Ang-2 were also downregulated in PMSN-VP and PMSN-VP@PPCeO$_2$ NP groups. Additionally, Ang-2 is a crucial marker in angiogenic sprouting, maturation and homeostasis and will inhibit vascular leakage from the CNV lesions through modulating Tie2 activation [44]. For patients suffering from an incomplete response to anti-VEGF therapy in nAMD, Ang-2 has become a potential target for nAMD therapy since VEGF and Ang-2 co-regulate pathological neovascularization [4,45]. Overall, our collective evidence elucidates that in the VP-containing NPs, CTGF and Ang-2 are acting as the downstream YAP effectors to mediate angiogenesis.

4. Conclusions

Emerging evidence has shown that in addition to VEGF, oxidative stress and inflammation also play **critical** roles in the pathogenesis of CNV. Hence, a combinational therapeutic strategy is urgently demanded for the treatment of nAMD. In this work, an integrated nano-drug delivery system with ROS-responsive properties was developed for choroidal neovascularization treatment. The boric acid ester bond between PMSN-VP and PPCeO$_2$ endowed the system with an ROS-responsive property, which was confirmed by the *in vitro* degradation and VP release results of NPs. Additionally, our *in vitro* data showed that the VP released from PMSN-VP@PPCeO$_2$ NPs inhibited the migration, and invasion of HUVECs and reduced the expression of angiogenesis-related factors by inhibiting the nuclear translocation of YAP. Moreover, the released CeO$_2$ NPs showed robust antioxidant and anti-inflammatory activities over BV2 cells. Notably, the PMSN-VP@PPCeO$_2$ NPs significantly reduced vascular leakage and macrophage infiltration in the CNV lesions. In conclusion, the combination effects of VP and CeO$_2$ together contribute to the effective treatment against CNV and provide a promising alternative for clinical nAMD applications.

CRediT authorship contribution statement

Jiayi Zuo: Writing – original draft, Methodology, Formal analysis. **Yining Pan:** Methodology, Formal analysis, Data curation. **Yuanli Wang:** Supervision, Formal analysis. **Wei Wang:** Validation, Software. **Haojie Zhang:** Methodology, Formal analysis. **Si Zhang:** Project administration, Funding acquisition. **Youru Wu:** Validation. **Jiangfan Chen:** Writing – review & editing, Project administration, Conceptualization. **Qingqing Yao:** Writing – review & editing, Project administration, Funding acquisition, Conceptualization.

Declaration of competing interest

The authors declare that they have no known competing financial interests or personal relationships that could have appeared to influence the work reported in this paper.

Acknowledgments

This research was supported by Zhejiang Provincial Natural Science Foundation of China under Grant (No. ZCLTGY24E0302), GuangDong

Basic and Applied Basic Research Foundation (2021A1515110131) and the Project of State Key Laboratory of Ophthalmology, Optometry and Visual Science, Wenzhou Medical University (NO. K03-20220203).

Appendix A. Supplementary data

Supplementary data to this article can be found online at https://doi.org/10.1016/j.mtbio.2025.101757.

Data availability

Data will be made available on request.

References

[1] W.L. Wong, X.Y. Su, X. Li, C.M.G. Cheung, R. Klein, T.Y. Wong, Lancet Global Health 2 (2014) E106.
[2] R. Flores, Á. Carneiro, M. Vieira, S. Tenreiro, M.C. Seabra, Ophthalmologica 224 (2022) 495.
[3] A. Lioecz, L. Miller, I. Kovacs, C. Czakó, T. Csipo, J. Baffi, A. Csiszar, S. Tarantini, Z. Ungvari, A. Yabluchanskiy, S. Conley, Geroscience 41 (2019) 813.
[4] P.S. Mettu, M.J. Allingham, S.W. Cousins, Prog. Retin. Eye Res. 82 (2021) 100906.
[5] Y. Ruan, S.B. Jiang, A. Gericke, Int. J. Mol. Sci. 22 (2021) 1296.
[6] N. Kushwah, K. Bora, M. Maurya, M.C. Pavlovich, J. Chen, Antioxidants 12 (2023) 1379.
[7] A. Arrigo, E. Aragona, F. Bandello, Asia-Pac. J. Ophthalmo. 12 (2024) 158.
[8] S.B. Farrokhran, Y. Qin, M.F. Bellver, Y.Q. Niu, I.A. Bhutto, S.A. Domingo, C. Y. Guo, M. Rodrigues, T. Domashevich, M. Deshpande, H. Megarity, R. Chopde, C. G. Eberhart, V.C. Soler, S. Montaner, A. Sodhi, PANS (Pest. Artic. News Summ.) 120 (2023) e2302845120.
[9] R. Terao, T. Ahmed, A. Suzumura, H. Terasaki, Antioxidants 11 (2022) 2189.
[10] G. Kaur, N.K. Singh, Int. J. Mol. Sci. 23 (2022) 386.
[11] W. Tan, J.L. Zou, S. Yoshida, B. Jiang, Y.D. Zhou, Int. J. Biol. Sci. 16 (2020) 2989–3001.
[12] G.T.K. Boopathy, W.J. Hong, Front. Cell Dev. Biol. 7 (2019) 49.
[13] J. Kim, Y.H. Kim, J. Kim, D.Y. Park, H. Bae, D.H. Lee, K.H. Kim, S.P. Hong, S. P. Jang, Y. Kubota, K.G. Kwon, D.S. Lim, G.Y. Koh, J. Clin. Investig. 127 (2017) 3447.
[14] J.M. Collins, A. Lang, C. Parisi, Y. Moharrer, M.P. Nijsure, J.H. Kim, S. Ahmed, G. L. Szeto, L. Qin, R. Gottardi, N.A. Dyment, N.C. Nowlan, J.D. Boerckel, Dev. Cell 59 (2024) 2.
[15] R.B. Mokhtari, N. Ashayeri, L. Bghaie, M. Sambi, K. Satari, N. Balucn, D.A. Bosykh, M.R. Szewczuk, S. Chakraborty, Cancers 15 (2023) 3468.
[16] S. Moon, S. Lee, J.A. Caesar, S. Pruchenko, A. Leask, J.A. Knowles, J. Sinon, B. Chaqour, iScience 23 (2020) 101184.
[17] S. Lee, A. Ahad, M. Luu, S. Moon, J. Caesar, W.V. Cardoso, M.B. Grant, B. Chaqour, Mol. Cell Biol. 39 (2019) e00107–e00119.
[18] H. Park, A. Shiva, P. Cummings, S. Kim, S. Kim, E. Lee, A. Leong, S. Chowdhury, C. Shawber, R. Carvajal, G. Thurston, J.Y. An, A.W. Lund, H.W. Yang, M. Kim, Cancer Res. 83 (2023) 1968.
[19] H.J. Choi, H. Zhang, H. Park, K.S. Choi, H.W. Lee, V. Agrawal, Y.M. Kim, Y. G. Kwon, Nat. Commun. 6 (2015) 6943.
[20] X.H. Wang, A.F. Valls, G. Schermann, Y. Shen, I.M. Moya, L. Castro, S. Urban, G. M. Solecki, F. Winkler, L. Riedemann, R.K. Jain, M. Mazzone, T. Schmidt, T. Fischer, G. Halder, C.R. de Almodóvar, Dev. Cell 42 (2017), 462-+.
[21] X. Yang, R. Zou, X.C. Dai, X.Y. Wu, F. Yuan, Y.F. Feng, Exp. Cell Res. 417 (2022) 113221.
[22] T.T. Zhao, J.N. Li, Y.B. Wang, X.J. Guo, Y. Sun, Ann. Med. 55 (2023) 2227424.
[23] S.J. Keam, L.J. Scott, M.P. Curran, Drugs 63 (2003) 2521.
[24] H.L. Wei, F.H. Wang, Y. Wang, T. Li, P. Xiu, J.T. Zhong, X.Y. Sun, J. Li, Cancer Sci. 108 (2017) 478.
[25] L. Lin, Y. Zheng, Q.Y. Li, Y.N. Sun, Y.W. Huang, L.L. Liang, L.M. Xu, Y.E. Zhao, Exp. Eye Res. 238 (2024) 109747.
[26] P.T. Nguyen, J. Lee, A. Cho, M.S. Kim, D. Choi, J.W. Han, M.I. Kim, J. Lee, Adv. Funct. Mater. 32 (2022) 2112428.
[27] B. Yuan, Z.C. Tan, Q. Guo, X.T. Shen, C. Zhao, J.L. Chen, Y.K. Peng, ACS Nano 17 (2023) 17383.
[28] A. Tisi, F. Pulcini, G. Carozza, V. Mattei, V. Flati, M. Passacantando, C. Antognelli, R. Maccarone, S. Delle Monache, Antioxidants 11 (2022) 1133.
[29] F. Muhammad, F.T. Huang, Y. Cheng, X.W. Chen, Q. Wang, C.X. Zhu, Y.H. Zhang, P. Wang, H. Wei, ACS Nano 16 (2022) 20567.
[30] Y.G. Kim, Y. Lee, N. Lee, M. Soh, D. Kim, T. Hyeon, Adv. Mater. 36 (2024) 10.
[31] V. Baldim, F. Bedioui, N. Mignet, I. Margaill, J.F. Berret, Nanoscale 10 (2018) 6971.
[32] S.T. Xu, K.X. Cui, K.Q. Long, J. Li, N. Fan, W.C. Lam, X.L. Liang, W.P. Wang, Adv. Sci. 10 (2023) 31.
[33] D.W. Kang, C.K. Kim, H.G. Jeong, M. Soh, T. Kim, I.Y. Choi, S.K. Ki, D.Y. Kim, W. Yang, T. Hyeon, S.H. Lee, Nano Res. 10 (2017) 2743.
[34] A.L. Elaimy, A.M. Mercurio, Sci. Signal. 11 (2018) eaau1165.
[35] Y.T. Ong, J. Andrade, M. Armbruster, C.Y. Shi, M. Castro, A.S.H. Costa, T. Sugino, G. Eelen, B. Zimmermann, K. Wilhelm, J. Lim, S. Watanabe, S. Guenther, A. Schneider, F. Zanconato, M. Kaulich, D.J. Pan, T. Braun, H. Gerhardt, A. Efeyan, P. Carmeliet, S. Piccolo, A.R. Grosso, M. Potente, Nat. Metab. 4 (2022), 672-+.
[36] R. Daley, V. Mddipatla, S. Ghosh, O. Chowdhury, S. Hose, J.S. Zigler, D. Sinha, H. T. Liu, Cell Death Discov. 9 (2023) 243.
[37] B. Bao, J.P. Liu, T.L. Li, Z.H. Yang, G.M. Wang, J.Z. Xin, H.S. Bi, D.D. Guo, Arch. Biochem. Biophys. 743 (2023) 109663.
[38] M. Fleckenstein, T.D.L. Keenan, R.H. Guymer, U. Chakravarthy, S. Schmitz-Valckenberg, C.C. Klaver, W.T. Wong, E.Y. Chew, Nat. Rev. Dis. Primers 7 (2021) 31.
[39] Z.Y. Li, H. Zhang, Y.J. Sun, Z.Z. Feng, B.J. Cui, J.X. Han, Y.N. Li, H.J. Liu, T. Sun, iScience 26 (2023) 106721.
[40] H. Yao, H. Xu, M.X. Wu, W.L. Lei, L.J. Li, D.N. Liu, Z.G. Wang, H.T. Ran, H.F. Ma, X.Y. Zhou, Acta Biomater. 166 (2023) 536.
[41] S.P. Kambhampati, I.A. Bhutto, T. Wu, K. Ho, D.S. McLeod, G.A. Lutty, R. M. Kannan, J. Contr. Release 335 (2021) 527.
[42] K. Kaarniranta, H. Uusitalo, J. Blasiak, S. Felszeghy, R. Kannan, A. Kauppinen, A. Salminen, D. Sinha, D. Ferrington, Prog. Retin. Eye Res. 79 (2020) 100858.
[43] S.B. Wang, X.R. Wang, Y.Q. Cheng, W.J. Ouyang, X. Sang, J.H. Liu, Y.R. Su, Y. Liu, C.Y. Li, L. Yang, L. Jin, Z.C. Wang, Oxid. Med. Cell. Longev. 2019 (2019) 3632169.
[44] J. Kim, J.R. Park, J. Choi, I. Park, Y. Hwang, H. Bae, Y. Kim, W. Choi, J.M. Yan, S. Han, T.Y. Chung, P. Kim, Y. Kubota, H.G. Augustin, W.Y. Oh, G.Y. Koh, Sci. Adv. 5 (2019) eaau6732.
[45] L.F. Desideri, C.E. Traverso, M. Nicolo, Expert Opin. Ther. Targets 26 (2022) 145.